

Deterministic many-body dynamics with multifractal response

Yusuf Kasim¹ and Tomaž Prosen^{1,2}

¹*Faculty of Mathematics and Physics, University of Ljubljana, Jadranska 19, SI-1000 Ljubljana, Slovenia*

²*Institute of Mathematics, Physics and Mechanics, Jadranska 19, SI-1000 Ljubljana, Slovenia*

(Dated: December 2, 2024)

Dynamical systems can display a plethora of ergodic and ergodicity breaking behaviors, ranging from simple periodicity to ergodicity and chaos. Here we report an unusual type of non-ergodic behavior in a many-body discrete-time dynamical system, specifically a multi-periodic response with multi-fractal distribution of equilibrium spectral weights at all rational frequencies. This phenomenon is observed in the momentum-conserving variant of the newly introduced class of the so-called parity check reversible cellular automata, which we define with respect to an arbitrary bipartite lattice. Although the models display strong fragmentation of phase space of configurations, we demonstrate that the effect qualitatively persists within individual fragmented sectors, and even individual typical many-body trajectories. We provide detailed numerical analysis of examples on 2D (honeycomb, square) and 3D (cubic) lattices.

Introduction.— The ergodic hypothesis formulated by Boltzmann in the late 19th century, the main assertion of which is an equivalence between time and statistical ensemble averages, is one of the key principles laying the mathematical foundation of statistical mechanics developed by Birkhoff, Von Neumann and others [1]. Nevertheless, the richness of dynamical behavior of generic deterministic or Hamiltonian systems to date could not be captured by a unified and rigorous mathematical theory. In the 1950s, the famous Fermi-Pasta-Ulam-Tsingou model demonstrated that the ergodic hypothesis can not always hold [2] and paved the way to the development of the theory of solitons and integrable models. Furthermore, the Kolmogorov-Arnold-Moser (KAM) theory shows that generic Hamiltonian systems are neither integrable, nor ergodic [3]. One can classify dynamical systems on the basis of the interplay of determinism and randomness, building a mathematical structure of the so-called ergodic hierarchy [4, 5]. However, in order to have the physical picture, one should also consider and classify possible effects of ergodicity breaking, which is linked to physical phenomena such as symmetry breaking, phase transitions, and spin glasses [6]. A system with broken ergodicity is confined to nontrivial subregions of phase space. This can be achieved by a structural mechanism such as free energy barriers or a dynamical mechanism by confining the time evolution by exact or approximate (cf. KAM tori) conserved quantities [7]. Understanding the physics of ergodicity breaking in classical many-body dynamics should have important implications to quantum many-body physics, where ergodic theory is much less developed. Nevertheless, it leads to important physical effects such as for instance: anomalous linear response and transport [8–11], quantum scars [12–14], fragmentation [15, 16], time-crystals [17–19], non-stationary dynamics and time-periodic equilibrium states [20].

One of the more recent venues of studying many-body dynamics and non-equilibrium statistical mechanics is reversible cellular automata [21, 22]. They may support a plethora of different behavior between integrable

and chaotic (ergodic) cellular automata, and have been used to provide exact solutions and analytical insights to transport and thermalization dynamics in interacting many-body systems [23–31]. More recently, they have been crucial to the understanding of a universality class of anomalous fluctuations in integrable systems [32, 33].

Here we report the discovery of a class of discrete phase space deterministic reversible many-body systems — parity check cellular automata on regular lattices (in two or more dimensions), with non-ergodic dynamics having multifractal dynamical structure factor and power-law distributions of AC Drude weights [34] at all rational frequencies. While cellular automata have been used before for constructing fractal or multifractal trajectories growing from specific initial conditions (non-equilibrium quench problem at zero entropy) [35–38], we observe here multifractal equilibrium dynamics (at finite entropy density). From a large-scale hydrodynamic (or thermodynamic) perspective, our models describe a kind of multi-scale glass in fundamental distinction to seemingly similar HPP or HPF cellular automata [39–41] which model regular Euler hydrodynamics.

Parity check automata.— Here we introduce a class of dynamical systems with discrete state space studied in this work. Let $G = (V, E)$ be an undirected bipartite graph with 2-component set of vertices $V = A \cup B$, $A \cap B = \emptyset$, such that each vertex $v \in A$ (B) joins $n = n(v)$ vertices in B (A) via edges $e(v) = (e_1, \dots, e_n)$. We assign dynamical degree of freedom $s_e \in \mathbb{Z}_2$ to each of the $N = |E|$ edges, such that a configuration $\underline{s} \in \mathbb{Z}_2^N$ represents a unique state of cellular automaton, interpreting $\mathcal{C} = \mathbb{Z}_2^N$ as a space of all configurations, i.e. “the phase space”. To each vertex, we assign a one-to-one map $\Phi_v : \mathbb{Z}_2^n \rightarrow \mathbb{Z}_2^n$, for which at this point we only require to satisfy the parity check (PC) property

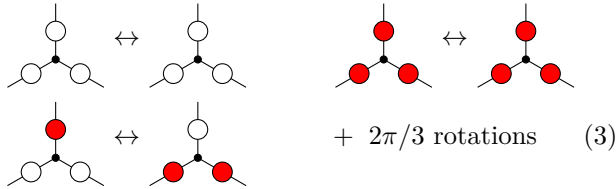
$$(s'_1 \dots s'_n) = \Phi_v(s_1 \dots s_n) \Rightarrow s_i + s_j = s'_i + s'_j \pmod{2}, \quad (1)$$

for all pairs $i, j \in \{1 \dots n\}$. We extend each local map Φ_v to \mathcal{C} acting trivially (as identity) on all other components. As all maps $\{\Phi_v\}_{v \in C}$ mutually commute for fixed $C =$

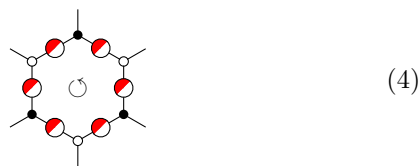
A, B , we define a reversible cellular automaton (discrete dynamical system) with the full one-step update rule

$$\Phi = \prod_{v \in B} \Phi_v \prod_{v \in A} \Phi_v, \quad \underline{s}(t+1) = \Phi(\underline{s}(t)). \quad (2)$$

It may be useful to embed the set of vertices in \mathbb{R}^d and think of an excitation on the edge/link e as a unit mass particle carrying one unit of momentum \vec{e} directed from v to the neighboring vertex v' . In this respect, we shall study only regular lattices where all possible momenta from each fixed vertex add to zero. Motivated by possible physics applications, we will then be interested in momentum conserving PC automata (MCPCA) for which $(s'_1 \dots s'_n) = \Phi_v(s_1 \dots s_n)$ implies $\sum_{e=1}^N s_e \vec{e} = -\sum_{e=1}^N s'_e \vec{e}$. For the simplest nontrivial bipartite lattice in $d = 2$, i.e. honeycomb lattice with coordination number $n = 3$ there is a unique nontrivial MCPCA defined by: $\Phi_v(s, s, s) = (s, s, s)$ and otherwise $\Phi_v(s, s', s'') = (\bar{s}, \bar{s}', \bar{s}'')$, where $\bar{s} = 1 - s$, illustrated graphically as



While classifying general PC and MCPC reversible cellular automata will be the subject of a separate study, we shall here only extend the above rule to arbitrary lattice or graph geometry with vertices of coordination number n as $\Phi_v(s, s \dots s) = (s, s \dots s)$ and otherwise $\Phi_v(s_1, s_2 \dots s_n) = (\bar{s}_1, \bar{s}_2 \dots \bar{s}_n)$, specifically for square lattice with $n = 4$ and cubic lattice ($d = 3$) with $n = 6$. Our MCPCA has several key properties: (i) It conserves d component total momentum vector $\vec{P}(\underline{s}) = \sum_{e=1}^N s_e \vec{e}$, $\vec{P} = \vec{P} \circ \Phi$. (ii) The parity of a sum of dynamical variables along any closed loop $\mathcal{L} = (e_1, e_2 \dots e_\ell)$, $\pi_{\mathcal{L}}(\underline{s}) = (-1)^{\sum_{i=1}^{\ell} s_{e_i}}$, is conserved $\pi_{\mathcal{L}} \equiv \pi_{\mathcal{L}} \circ \Phi$. (iii) If the classical spins along a closed loop \mathcal{L} are in a Néel configuration $(s_{e_1}, s_{e_2} \dots s_{e_\ell}) = (0, 1, 0, 1 \dots 0, 1)$ (ℓ even) then these spins are preserved at all times, i.e. the Néel loop is frozen [42]. All these properties follow from the definitions of the MCPCA. The property (ii) is particularly important: suppose a lattice with N edges has M independent closed loops, say along the smallest plaquettes like in the honeycomb lattice:



For honeycomb, square and cubic lattices, $M = N/3$, $M = N/2$, and $M = 5N/6$, respectively, so we expect

that \mathcal{C} fragments into 2^M sectors with fixed plaquette parities, leaving the components which still contain exponentially many, 2^{N-M} , configurations. We note that the properties (i) and (iii) do not significantly or qualitatively further reduce the size of fragmented components, which in any case remain exponential in N . For instance, we verified that the length of typical and longest periodic orbits are exponential in N .

All-periodic multifractal dynamical response.— Fundamental observables characterizing ergodic properties of a reversible cellular automaton are dynamical correlation functions of a local observable $\rho_v(\underline{s})$

$$C_{\vec{r}}(t) = \langle \rho_v(\underline{s}) \rho_{v+\vec{r}}(\Phi^{(t)}(\underline{s})) \rangle, \quad (5)$$

where $\langle A \rangle \equiv \sum_{\underline{s} \in \mathcal{C}} p(\underline{s}) A(\underline{s})$ and p represents an invariant (equilibrium) statistical state $p = p \circ \Phi$, $p(\underline{s}) \geq 0$, $\sum_{\underline{s}} p(\underline{s}) = 1$. Throughout this work, we will consider a maximum entropy (‘infinite temperature’) ensemble with $p(\underline{s}) = 1/|\mathcal{C}| = 2^{-N}$ and symmetrized local particle density $\rho_v(\underline{s}) = \sum_{i=1}^{n(v)} s_{e_i(v)} - n(v)/2$ satisfying $\langle \rho_v \rangle = 0$. Here \vec{r} denotes a valid displacement between a vertex v and another vertex in the Euclidean embedding. The simplest and most informative is the local autocorrelator $\vec{r} = 0$ which we will characterize in terms of a spectral function

$$S(\omega) = \sum_{t \in \mathbb{Z}} C_{\vec{0}}(t) \exp(2\pi i t \omega). \quad (6)$$

Allowing for the possibility that the system has a sub-harmonic response at any integer periodicity we can write the spectral function as:

$$S(\omega) = \sum'_{n,p} A_{n,p} \delta\left(\omega - \frac{n}{p}\right) + S_{\text{reg}}(\omega), \quad (7)$$

where the sub-harmonic AC ‘Drude weights’ read

$$A_{n,p} = \lim_{T \rightarrow \infty} \frac{1}{T} \sum_{t=0}^{T-1} C_{\vec{0}}(t) \exp\left(-\frac{2\pi i t n}{p}\right). \quad (8)$$

The sum $\sum'_{n,p}$ runs over $n, p \in \mathbb{Z}$, $|n| < p$, with n, p coprime. In general, for ergodic and mixing dynamics, all $A_{n,p} \equiv 0$. For non-ergodic dynamics, $A_{0,1} \neq 0$, while for p -periodic dynamics (aka time crystal with p -subharmonic response [19]), $A_{n,p} \neq 0$ for some n .

We define dynamics to be *infinite-periodic* if for some (local) observable infinitely many $A_{n,p} \neq 0$, and *all-periodic* if $A_{n,p} \neq 0$ for all coprime n, p . As we shall demonstrate below, MCPCA represents a wide class of all-periodic dynamics, in the thermodynamic limit $N \rightarrow \infty$, with multifractal spectral distributions $S(\omega)$.

Results.— We ran extensive Monte-Carlo simulations of the spectral function $S(\omega)$ for different regular bipartite lattices in $d = 2, 3$, honeycomb, square and cubic. We sampled initial configurations either fully randomly, i.e. considered flat equilibrium state $p(\underline{s}) = 2^{-N}$, or we

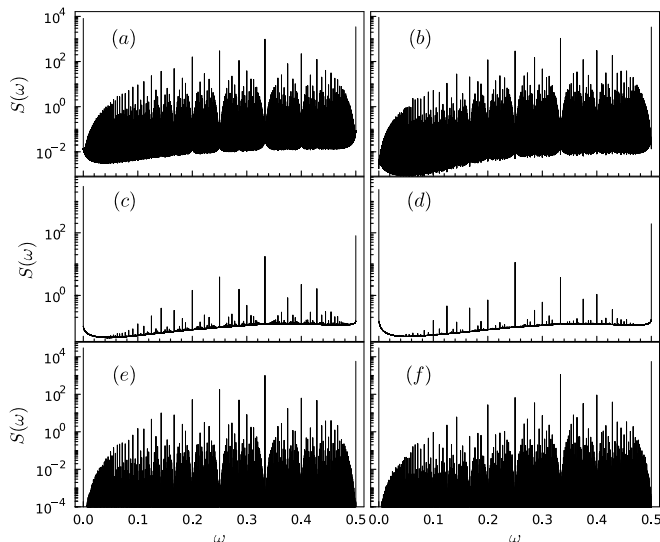


FIG. 1. The power spectra of the density-density correlation function $S(\omega)$. All the plots are calculated for $T = 2^{20}$ and using a Gaussian filter (see text for details). We show data for 16×16 square lattice, $N = 2 \times 16^2$, in the random loop-parity sector (a) averaging over $\mathcal{N} = 0.68 \cdot 10^6$ random initial conditions, and in all-positive loop-parity sector (b) with $\mathcal{N} = 0.80 \cdot 10^6$; for 16×16 -vertex honeycomb lattice, $N = (3/2) \times 16^2$, within random (c), and all-positive (d) loop-parity sector, both with $\mathcal{N} = 2.8 \cdot 10^6$; and finally, for $8 \times 8 \times 8$ cubic lattice, $N = 3 \times 8^3$, within random (e) ($\mathcal{N} = 1.2 \cdot 10^6$), and all-positive (f) ($\mathcal{N} = 0.65 \cdot 10^6$) loop parity sector.

considered a subsector of equally weighted 2^M configurations with all loop parities $\pi_L = +1$. These data sets are respectively labeled by $\pi = \pm$ and $\pi = +$. In order to be able to resolve possible delta singularities in $S(\omega)$ more reliably, we use a Gaussian filtering of very long signals, $T = 2^{20}$, and compute power spectrum as $S(\nu/T) = \sum_{t=0}^{T-1} C_{\bar{0}}(t) e^{-16(t/T-1/2)^2 + 2\pi i t \nu/T}$, $\nu = -\frac{T}{2}, -\frac{T}{2} + 1, \dots, \frac{T}{2} - 1$, using Fast Fourier Transform and average over \mathcal{N} (typically $\mathcal{N} \approx 10^6$) initial configurations. The results are shown in Fig. 1 and have been checked to be practically insensitive to system size once the number of edges N exceeded a few hundred or so. Remarkably, the result is also robust if we replace the ensemble average by a time average of $S(\omega)$ computed over long sections of even longer fixed, typical trajectory (for sufficiently large N), as shown in [43]. This means that $S(\omega)$, despite being a highly singular and irregular object, behaves like an ergodic observable in a fixed loop-parity phase space sector.

We observe a clear evidence of delta-spikes at all rational frequencies in all $S(\omega)$. Due to Gaussian filtering it was possible to reliably determine the weights $A_{n,p}$ for periods up to $p \approx 300$ by polynomial $\varepsilon \rightarrow 0$ extrapolations of $\int_{n/p-\varepsilon}^{n/p+\varepsilon} d\omega S(\omega) = A_{n,p} + A'_{n,p}\varepsilon + \dots$. Writing the total weight of period p as $B_p = \sum_n A_{n,p}$ we find a very

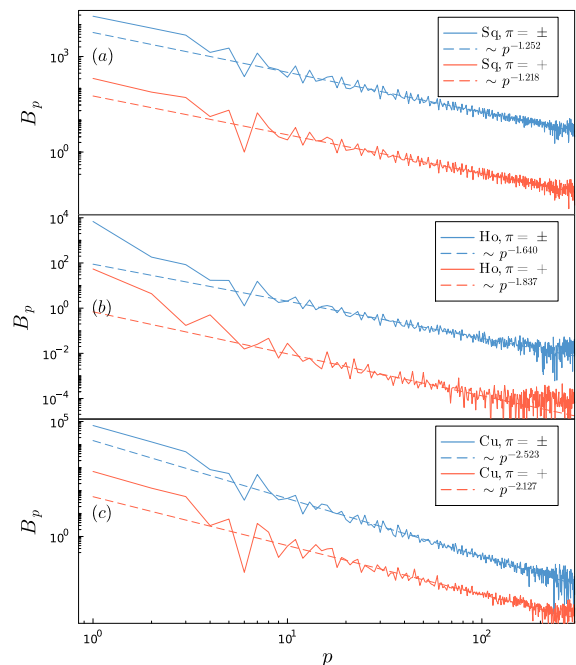


FIG. 2. Total period- p spectral weight $B_p = \sum_n A_{n,p}$ as a function of p for (a) square, (b) honeycomb, and (c) cubic lattices for random loop-parity ($\pi = \pm$, in blue) and for positive parity ($\pi = +$, in red) with best power law fits plotted in dashed (see legend). Note that the data for the positive loop-parity sector is shifted by factor 10^{-2} for better visualization. We used the data shown in Fig. 1 to produce these plots.

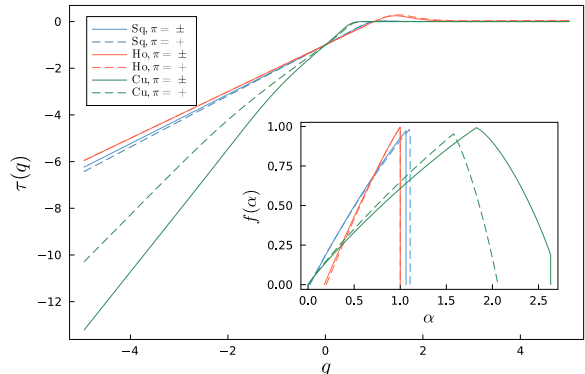


FIG. 3. Moment scaling exponent $\tau(q)$ for square (Sq), honeycomb (Ho), and cubic (Cu) lattices for random loop-parity ($\pi = \pm$, full lines) and all-positive loop-parity ($\pi = +$, dashed lines) sectors. The inset shows the singularity spectrum $f(\alpha)$. See main text and [43] for details of computation.

clear evidence of asymptotic power law scaling

$$B_p \asymp p^{-\mu}, \quad (9)$$

where the exponent μ depends only on the lattice geometry and phase space sector (see Fig. 2). We note that in all cases $\mu > 1$, so the total singular contribution to $S(\omega)$ converges. We also find a significant nonzero regular part

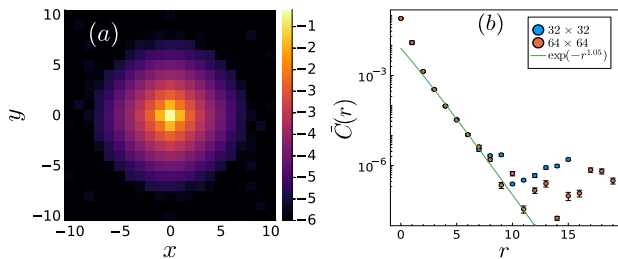


FIG. 4. (a) Heatmap of the time averaged density-density correlation function $\bar{C}(\vec{r})$ in log-10 scale for MCPCA on 64×64 square lattice. (b) Radial behavior of $\bar{C}(\vec{r})$ averaged over four directions $(r, 0)$, $(-r, 0)$, $(0, r)$, $(0, -r)$, and comparing two different lattice sizes, 32×32 (blue), and 64×64 (red) and best fitted exponential decay $e^{-1.05r}$ (green). For both lattice sizes, we averaged over $T = 2048$ consecutive time-steps and sampled over $\mathcal{N} \sim 10^6$ random initial conditions in the random parity sector $\pi = \pm$ (estimated statistical error bars indicated).

$S_{\text{reg}}(\omega)$, except in the cubic lattice case, where it could possibly vanish.

We also perform a multifractal scaling analysis of $S(\omega)$. Splitting the interval $\omega \in [0, 1]$ into $1/\varepsilon$ boxes of size ε , we denote the weight in the i -th interval as $P_i(\varepsilon) = \int_{i\varepsilon}^{(i+1)\varepsilon} d\omega S(\omega)$. We then define the standard τ -exponents as:

$$\tau(q) = \lim_{\varepsilon \rightarrow 0} \frac{\log \sum_i P_i^q(\varepsilon)}{\log \varepsilon} \quad (10)$$

where in practice we make sure that ε is much bigger than frequency resolution $1/T \ll \varepsilon \ll 1$. Finally, the generalized dimensions and multifractal spectrum are determined as $D(q) = \tau(q)/(q-1)$ and $f(\alpha) = \min_q(q\alpha - \tau(q))$, see Fig. 3 and [43] for details. We observe that the dynamics of MCPCA is in all cases characterized with multifractal dynamical response.

Finally, we attempt to analyze the spatial dependence of dynamical correlations $C_{\vec{r}}(t)$. While temporal dependencies seem to follow very similar multifractal behavior for any \vec{r} , their amplitude quickly decays with increasing displacement \vec{r} . In order to illustrate this we plot in Fig. 4 time-averaged spatially resolved correlator $\bar{C}(\vec{r}) = \frac{1}{T} \sum_{t=0}^{T-1} C_{\vec{r}}(t)$ and find a quick, possibly isotropic asymptotically exponential decay

$$\bar{C}(\vec{r}) \asymp e^{-|\vec{r}|/\xi}. \quad (11)$$

Therefore, MCPCA dynamics exhibits a combination of slow dynamics and long-range multifractal order in time with exponential damping in space. This makes it reminiscent of a sort of multiscale glass.

Conclusion.— We investigated a family of momentum conserving parity check automata (MCPCA) as many-body deterministic dynamical systems defined on extensive bipartite graphs. Clear numerical evidence has been provided for a multifractal dynamical response (dynamical structure factor) for models defined on various regular lattices in 2D and 3D. We showed that the response

is all-periodic, i.e. we observe subharmonic response at all (dense singular distribution of) rational frequencies, even for a typical fixed trajectory in (thermodynamically) large system. In the future, one should attempt to better understand the role of conserved charges and algebraic structures behind fractal dynamics and hierarchical fragmentation in these systems. We conclude that parity check automata exhibit previously unseen non-ergodic equilibrium states and offer a new mechanism of ergodicity breaking in non-disordered systems fundamentally distinct from integrability.

Most interestingly, the PCA offers direct generalization to quantum circuits or quantum cellular automata, where deterministic processes are replaced by parity-check-allowed unitary superpositions. Preliminary investigations indicate possible quantum transitions to/from non-ergodic and multifractal dynamics powered by quantum fluctuations/interference [42]. On the other hand, replacing unitary processes by stochastic transitions, i.e. investigating stochastic PCA, immediately kills multifractality and renders the response $S(\omega)$ smooth (see [43]).

Acknowledgements.— We thank Bruno Bertini, Alexei Kitaev, Katja Klobas, and Roderich Moessner for the fruitful discussions, as well as Pavel Orlov and Cheryne Jonay for their collaboration on a related follow-up project. All power spectra were calculated using the FFTW library [44]. The analysis of multifractal dimensions, τ exponents and singularity spectra followed the methods lined in [45, 46]. This research has received funding from the European Union's Horizon 2020 research and innovation programme under the Marie Skłodowska-Curie grant agreement number 95547, European Research Council (ERC) through Advanced grant QUEST (Grant Agreement No. 101096208), as well as the Slovenian Research and Innovation agency (ARIS) through the Program P1-0402.

-
- [1] G. G. Emch and C. Liu, Setting-up the ergodic problem, in *The Logic of Thermostatistical Physics* (Springer Berlin Heidelberg, Berlin, Heidelberg, 2002) pp. 237–259.
 - [2] E. Fermi, P. Pasta, S. Ulam, and M. Tsingou, Studies of the nonlinear problems, Technical report 10.2172/4376203 (1955).
 - [3] L. Markus and K. R. Meyer, *Generic Hamiltonian dynamical systems are neither integrable nor ergodic*, Memoirs of the American Mathematical Society, Vol. No. 144 (American Mathematical Society, Providence, RI, 1974) pp. iv+52.
 - [4] J. Berkovitz, R. Frigg, and F. Kronz, The ergodic hierarchy, randomness and hamiltonian chaos, *Studies in History and Philosophy of Science Part B: Studies in History and Philosophy of Modern Physics* **37**, 661 (2006).
 - [5] I. P. Cornfeld, S. V. Fomin, and Y. G. Sinai, *Ergodic theory*, Vol. 245 (Springer Science & Business Media, 2012).
 - [6] G. Venkataraman, D. Sahoo, and V. Balakrishnan, Ergodicity breaking, in *Beyond the Crystalline State: An Emerging Perspective* (Springer Berlin Heidelberg,

- Berlin, Heidelberg, 1989) pp. 117–124.
- [7] R. Palmer, Broken ergodicity, *Advances in Physics* **31**, 669 (1982), <https://doi.org/10.1080/00018738200101438>.
- [8] P. Mazur, Non-ergodicity of phase functions in certain systems, *Physica* **43**, 533 (1969).
- [9] X. Zotos, F. Naef, and P. Prelovsek, Transport and conservation laws, *Phys. Rev. B* **55**, 11029 (1997).
- [10] T. Prosen, Open xzx spin chain: Nonequilibrium steady state and a strict bound on ballistic transport, *Phys. Rev. Lett.* **106**, 217206 (2011).
- [11] B. Bertini, F. Heidrich-Meisner, C. Karrasch, T. Prosen, R. Steinigeweg, and M. Žnidarič, Finite-temperature transport in one-dimensional quantum lattice models, *Rev. Mod. Phys.* **93**, 025003 (2021).
- [12] E. J. Heller, Bound-state eigenfunctions of classically chaotic hamiltonian systems: Scars of periodic orbits, *Phys. Rev. Lett.* **53**, 1515 (1984).
- [13] L. Kaplan, Scars in quantum chaotic wavefunctions, *Nonlinearity* **12**, R1 (1999).
- [14] C. Turner, A. Michailidis, D. Abanin, M. Serbyn, and Z. Papić, Weak ergodicity breaking from quantum many-body scars, *Nature Physics* **14**, 745 (2018).
- [15] P. Sala, T. Rakovszky, R. Verresen, M. Knap, and F. Pollmann, Ergodicity breaking arising from hilbert space fragmentation in dipole-conserving hamiltonians, *Phys. Rev. X* **10**, 011047 (2020).
- [16] S. Moudgalya, B. A. Bernevig, and N. Regnault, Quantum many-body scars and hilbert space fragmentation: a review of exact results, *Rep. Prog. Phys.* **85**, 086501 (2022).
- [17] F. Wilczek, Quantum time crystals, *Phys. Rev. Lett.* **109**, 160401 (2012).
- [18] V. Khemani, A. Lazarides, R. Moessner, and S. L. Sondhi, Phase structure of driven quantum systems, *Phys. Rev. Lett.* **116**, 250401 (2016).
- [19] M. P. Zaletel, M. Lukin, C. Monroe, C. Nayak, F. Wilczek, and N. Y. Yao, Colloquium: Quantum and classical discrete time crystals, *Rev. Mod. Phys.* **95**, 031001 (2023).
- [20] B. Buča, Unified theory of local quantum many-body dynamics: Eigenoperator thermalization theorems, *Phys. Rev. X* **13**, 031013 (2023).
- [21] S. Takesue, Reversible cellular automata and statistical mechanics, *Phys. Rev. Lett.* **59**, 2499 (1987).
- [22] A. Bobenko, M. Bordemann, C. Gunn, and U. Pinkall, On two integrable cellular automata, *Communications in mathematical physics* **158**, 127 (1993).
- [23] B. Buča, K. Klobas, and T. Prosen, Rule 54: exactly solvable model of nonequilibrium statistical mechanics, *Journal of Statistical Mechanics: Theory and Experiment* **2021**, 074001 (2021).
- [24] M. Medenjak, K. Klobas, and T. Prosen, Diffusion in deterministic interacting lattice systems, *Phys. Rev. Lett.* **119**, 110603 (2017).
- [25] T. Prosen and C. Mejía-Monasterio, Integrability of a deterministic cellular automaton driven by stochastic boundaries, *J. Phys. A: Math. and Theor.* **49**, 185003 (2016).
- [26] K. Klobas and T. Prosen, On two reversible cellular automata with two particle species, *J. of Phys. A: Math. and Theor.* **55**, 094003 (2022).
- [27] K. Klobas, B. Bertini, and L. Piroli, Exact thermalization dynamics in the “rule 54” quantum cellular automaton, *Phys. Rev. Lett.* **126**, 160602 (2021).
- [28] J. W. P. Wilkinson, K. Klobas, T. Prosen, and J. P. Garahan, Exact solution of the floquet-pxp cellular automaton, *Phys. Rev. E* **102**, 062107 (2020).
- [29] T. Gombor and B. Pozsgay, Superintegrable cellular automata and dual unitary gates from Yang-Baxter maps, *SciPost Phys.* **12**, 102 (2022).
- [30] T. Prosen, On two non-ergodic reversible cellular automata, one classical, the other quantum, *Entropy* **25**, 739 (2023).
- [31] R. Sharipov, M. Koterle, S. Grozdanov, and T. Prosen, To be published.
- [32] Ž. Krajnik, J. Schmidt, V. Pasquier, E. Ilievski, and T. Prosen, Exact anomalous current fluctuations in a deterministic interacting model, *Phys. Rev. Lett.* **128**, 160601 (2022).
- [33] Ž. Krajnik, J. Schmidt, V. Pasquier, T. Prosen, and E. Ilievski, Universal anomalous fluctuations in charged single-file systems, *Phys. Rev. Res.* **6**, 013260 (2024).
- [34] M. Medenjak, T. Prosen, and L. Zadnik, Rigorous bounds on dynamical response functions and time-translation symmetry breaking, *SciPost Phys.* **9**, 003 (2020).
- [35] J. Nagler and J. C. Claussen, $1/f^\alpha$ spectra in elementary cellular automata and fractal signals, *Phys. Rev. E* **71**, 067103 (2005).
- [36] J. S. Murguía, J. E. Pérez-Terrazas, and H. C. Rosu, Multifractal properties of elementary cellular automata in a discrete wavelet approach of mf-dfa, *Europhysics Letters* **87**, 28003 (2009).
- [37] Y. Hayase and T. Ohta, Self-replicating pulses and sierpinski gaskets in excitable media, *Phys. Rev. E* **62**, 5998 (2000).
- [38] J. C. Claussen, J. Nagler, and H. G. Schuster, Sierpinski signal generates $1/f^\alpha$ spectra, *Phys. Rev. E* **70**, 032101 (2004).
- [39] J. Hardy, Y. Pomeau, and O. de Pazzis, Time evolution of a two-dimensional model system. I. Invariant states and time correlation functions, *J. Math. Phys.* **14**, 1746 (1973).
- [40] J. Hardy, O. de Pazzis, and Y. Pomeau, Molecular dynamics of a classical lattice gas: Transport properties and time correlation functions, *Phys. Rev. A* **13**, 1949 (1976).
- [41] U. Frisch, B. Hasslacher, and Y. Pomeau, Lattice-gas automata for the navier-stokes equation, *Phys. Rev. Lett.* **56**, 1505 (1986).
- [42] P. Orlov, Y. Kasim, C. Jonay, and T. Prosen, To be published.
- [43] Supplemental material associated with this manuscript.
- [44] M. Frigo and S. G. Johnson, The design and implementation of FFTW3, *Proceedings of the IEEE* **93**, 216 (2005), special issue on “Program Generation, Optimization, and Platform Adaptation”.
- [45] A. Chhabra and R. V. Jensen, Direct determination of the $f(\alpha)$ singularity spectrum, *Phys. Rev. Lett.* **62**, 1327 (1989).
- [46] J. Martin, I. García-Mata, O. Giraud, and B. Georgeot, Multifractal wave functions of simple quantum maps, *Phys. Rev. E* **82**, 046206 (2010).

Supplemental material for “Deterministic many-body dynamics with multifractal response”

In this supplemental material, we provide additional demonstrations and numerical evidence on various dynamical and ergodic features of parity check automata, specifically MCPCA and some of their modifications/deformations.

Firstly, we graphically illustrate MCPCA dynamics on the square and hexagonal lattice enhancing dynamically active regions of particle configurations in real space and demonstrating their very slow deterministic percolation.

Secondly, we illustrate the multifractal power spectrum $S(\omega)$ for a global, spatially extensive observable, and demonstrate its similarity to the power spectrum for a local observable (analyzed in the main text).

Thirdly, we demonstrate an effective ergodicity of dynamical structure factor $S(\omega)$ by comparing phase space (initial state) averages with an average over sections of a long, fixed, typical trajectory.

Fourth, we define stochastic deformation of MCPCA and demonstrate that multifractality of $S(\omega)$ washes away continuously by increasing the stochastic jump probabilities.

Fifth, we compare the power spectrum of MCPCA with an alternative PCA with similar rules but with broken momentum conservation, and find very similar multifractal structure.

Sixth, we provide additional information on generalized dimensions D_q of multifractal $S(\omega)$ for various lattice geometries.

Seventh, we plot a typical autocorrelation function for local density observable, graphically illustrating all-periodicity in real time.

SNAPSHOTS OF THE DYNAMICS

To give an insight into space-time dynamics, we plot snapshots of a typical trajectory on a 32×32 square lattice with periodic boundary condition of size $N = 2 \times 32^2$ (number of edges – link degrees of freedom) with random initial condition in the random loop-parity sector ($\pi = \pm$). We show 9 snapshots of the dynamics in Fig S1 up to $t = 10^6$ time-steps. We note that the snapshots are rotated by 45° with respect to the standard Cartesian grid. The value at each link of the lattice is depicted as a gray (0) or red (1) square. The brighter color indicate cells which have ever flipped from time 0 to a given time t . In this way we get an impression of the slow growth of dynamically active regions of space, which is reminiscent of a slow, deterministic percolation process.

One might wonder if such slow dynamics as observed in the square lattice rests behind the fundamental reason for multifractality. Hence, we plot in Fig. S2 similar snapshots for the honeycomb lattice. We see that here, probably due to lower coordination number, the dynamics appears much faster and that the domain of active cells quickly forms a percolating cluster and eventually covers a vast majority of the lattice unlike in the square lattice case. It seems therefore, although the dynamical lattice covering seems an interesting problem of its own, it is not qualitatively connected to multifractality and all-periodic response.

POWER SPECTRUM AND DYNAMICAL RESPONSE FOR A GLOBAL/EXTENSIVE OBSERVABLE

Here we show the dynamical response function – power spectrum $S(\omega)$ for an example of a global/extensive observable. Instead of looking at the density-density correlation function $C_{\vec{r}}(t)$ at $\vec{r} = 0$, we now take the autocorrelation function of global/total excitation number

$$C(t) = \langle R(\underline{s})R(\Phi^{(t)}(\underline{s})) \rangle. \quad (\text{S1})$$

The extensive, total excitation number (centered around zero) $R(\underline{s})$ is defined as:

$$R(\underline{s}) = \sum_v \rho_v(\underline{s}). \quad (\text{S2})$$

Straightforward calculation expresses $C(t)$ as a spatial sum of $C_{\vec{r}}(t)$

$$C(t) = \sum_{v,v'} C_{v-v'}(t). \quad (\text{S3})$$

Fig S3 shows the power spectrum $S(\omega)$ of the global correlation function $C(t)$ for the square lattice. We observe that the all-periodic multifractal response is (at least qualitatively) indistinguishable from the response for local

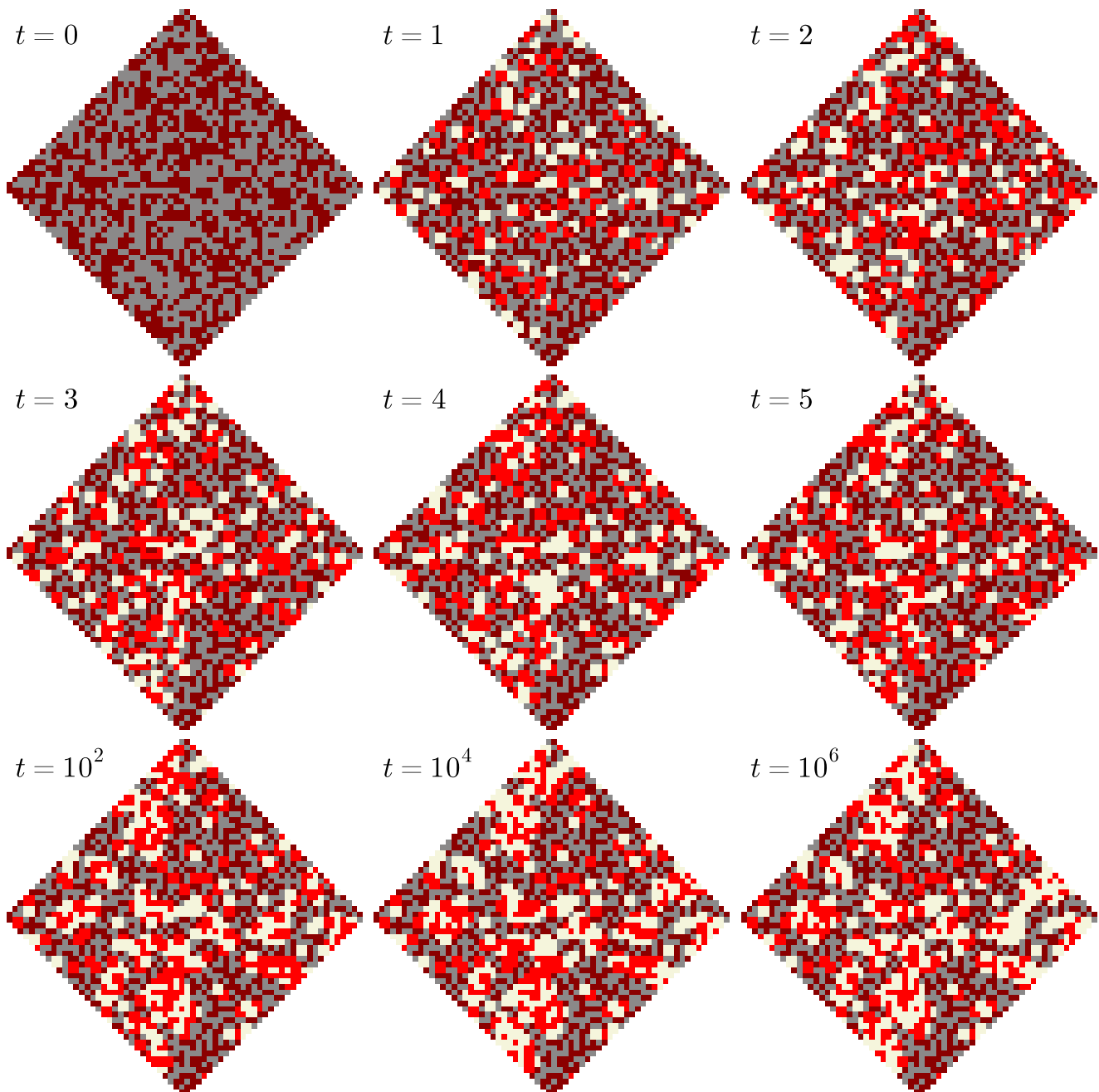


FIG. S1. Snapshots of the time evolution (time steps indicated in the figure) of a typical configuration for 32×32 square lattice with periodic boundary conditions and 2×32^2 link degrees of freedom, shown as gray/beige (0) or dark/light red (1) cells. The lighter colors indicate cells which experienced dynamics (at least one flip) up to a given time t , while darker colors represent frozen parts of the lattice space.

observable. Furthermore, the power-law decay of B_p for the global observable shown in fig S4 is within numerical accuracy identical as for the local observable. These results assure us that the multifractal response is not confined to the local observables, but the behavior is to be expected for generic local or global observables.

TIME AVERAGE OVER SINGLE LONG TRAJECTORY VS. PHASE SPACE AVERAGE

The MCPCA dynamics is clearly non-ergodic as exemplified by nonzero DC Drude weight $A_{0,1}$ for local and extensive observables. However, the computation of time-nonlocal observables may become ‘self-averaging’ with increasing the

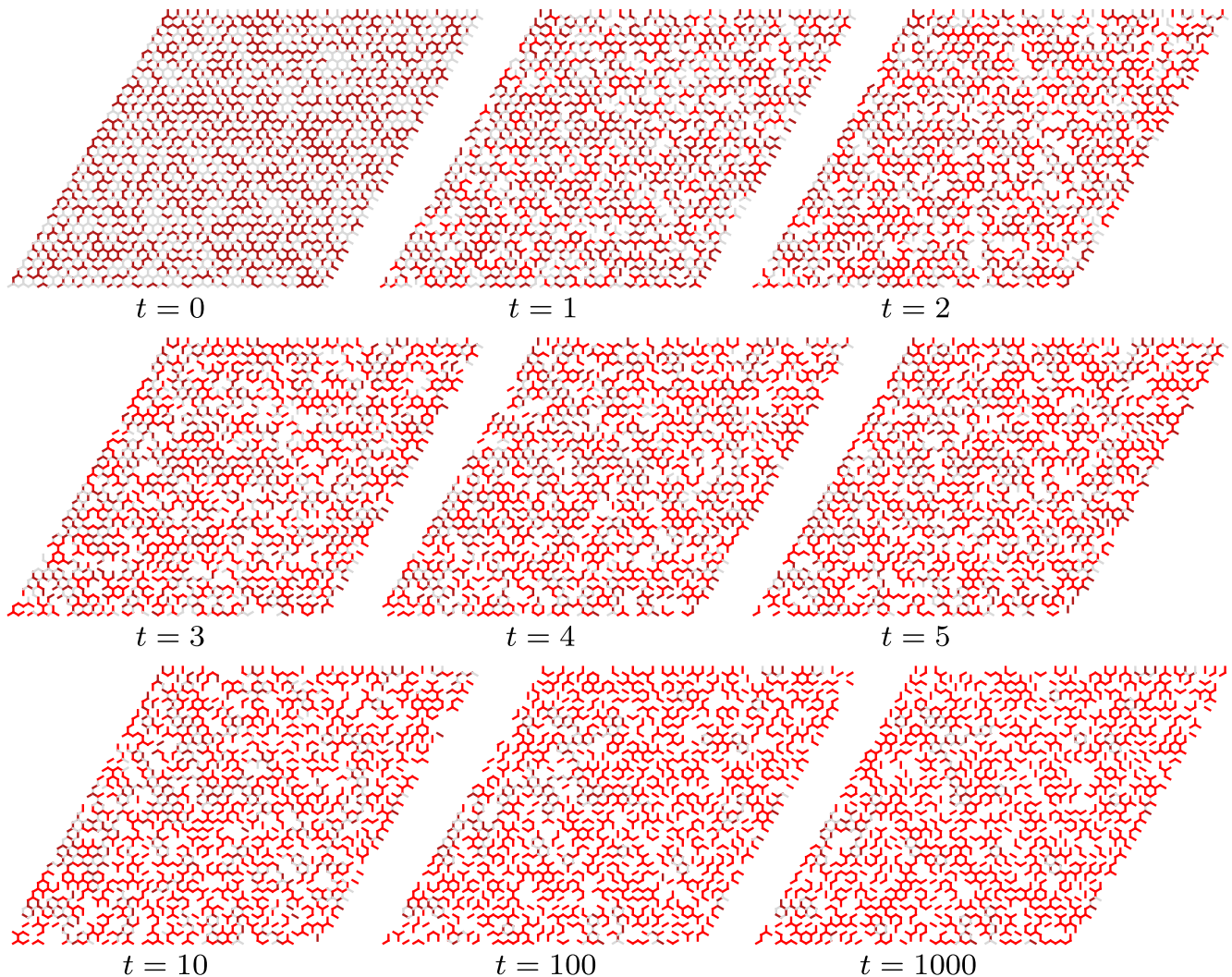


FIG. S2. Snapshots of the time evolution (time steps indicated in the figure) of a typical configuration for 32×32 honeycomb lattice with periodic boundary conditions and similar color coding as in the previous figure (gray/dark red representing inactive cells, white/light red cells representing dynamically active cells). As the cells are associated to links/edges of the honeycomb lattice, we plot them by thick lines.

system size and time of simulation. For instance, $S(\omega)$ calculated for a fixed, typical trajectory in a thermodynamically large system can uniformly sample configurations in smaller subsystems, and hence faithfully represent an ensemble (phase space) average. This is indeed suggested by Fig. 4 of the main text, indicating that the spatial correlations decay exponentially.

Here we focus on the square lattice as well. We take a lattice of size $L \times L$ with periodic boundary conditions and start from a typical, random trajectory with all positive loop-parities. Then we compute $S(\omega)$ as a time average over T_1 sections of length T_2 over a very long trajectory of length $T = T_1 T_2$. We find a clear indication of multifractal power spectrum as L and T_1, T_2 become sufficiently large, essentially very similar to the phase space average of $S(\omega)$. See Fig. S5 for comparison of results for $L = 128 \times 128$ and $L = 512 \times 512$ and sufficiently large T_1, T_2 .

It is clear from figure S5 that at large enough system sizes, the time averages agree with the average over the phase space. We note that for larger system sizes we have to sacrifice the sharpness of the data by taking shorter final times, this is due to the increase of simulation times as we increase system size. But even at our current resolution, we can see a good agreement for $L = 512 \times 512$ in comparison with $L = 128 \times 128$ where the amplitudes of peaks are different between the two averages.

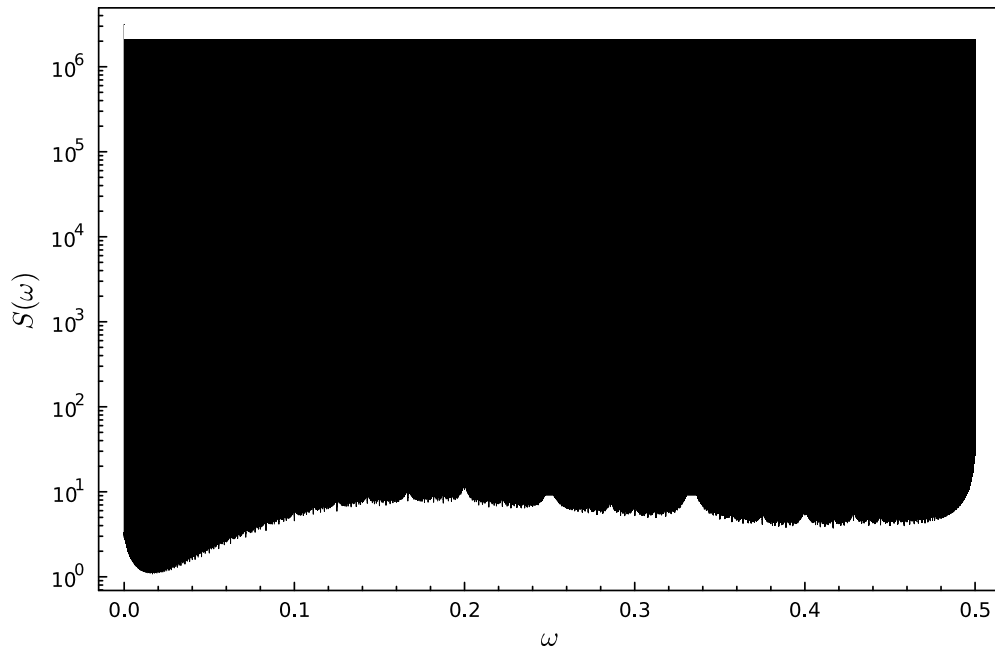


FIG. S3. Power spectra of the global (integrated, extensive) density-density correlation functions as a function of the frequency for 16×16 square lattice ($N = 2 \cdot 16^2$). The data is calculated for $T = 2^{20}$ and for $\mathcal{N} = 3.4 \cdot 10^5$ all in the random parity sector $\pi = \pm$.

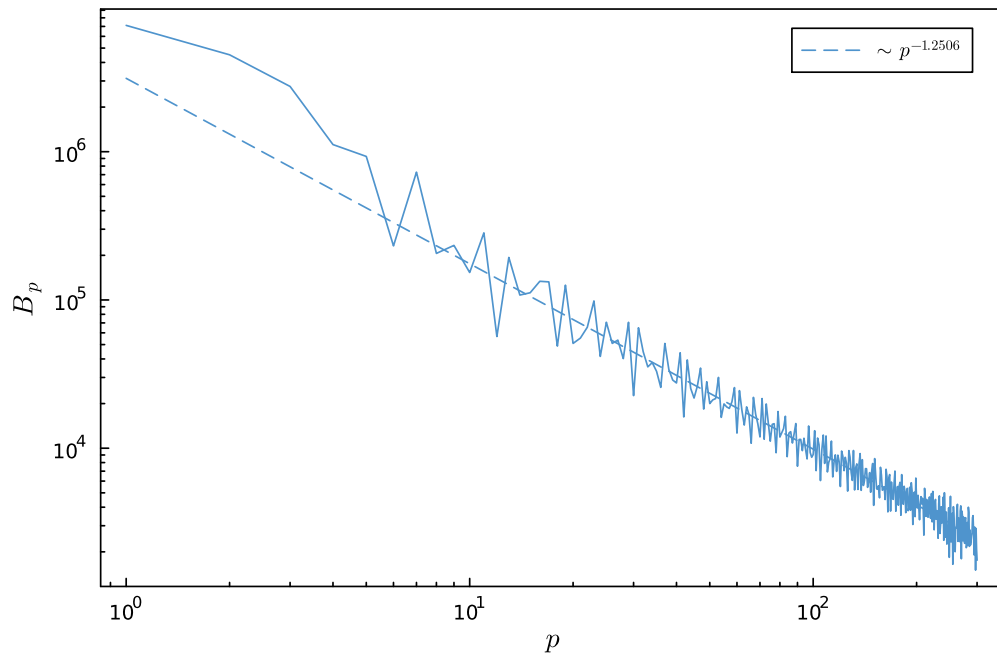


FIG. S4. B_p as a function of the period p in log scale for the global density-density correlation function for the square lattice.

POWER SPECTRUM OF STOCHASTICALLY DEFORMED MCPA

Here we check the robustness of our main finding, i.e. multifractality of the power spectrum, against a stochastic deformation of MCPA breaking deterministic and reversible character of the model. We again consider the square

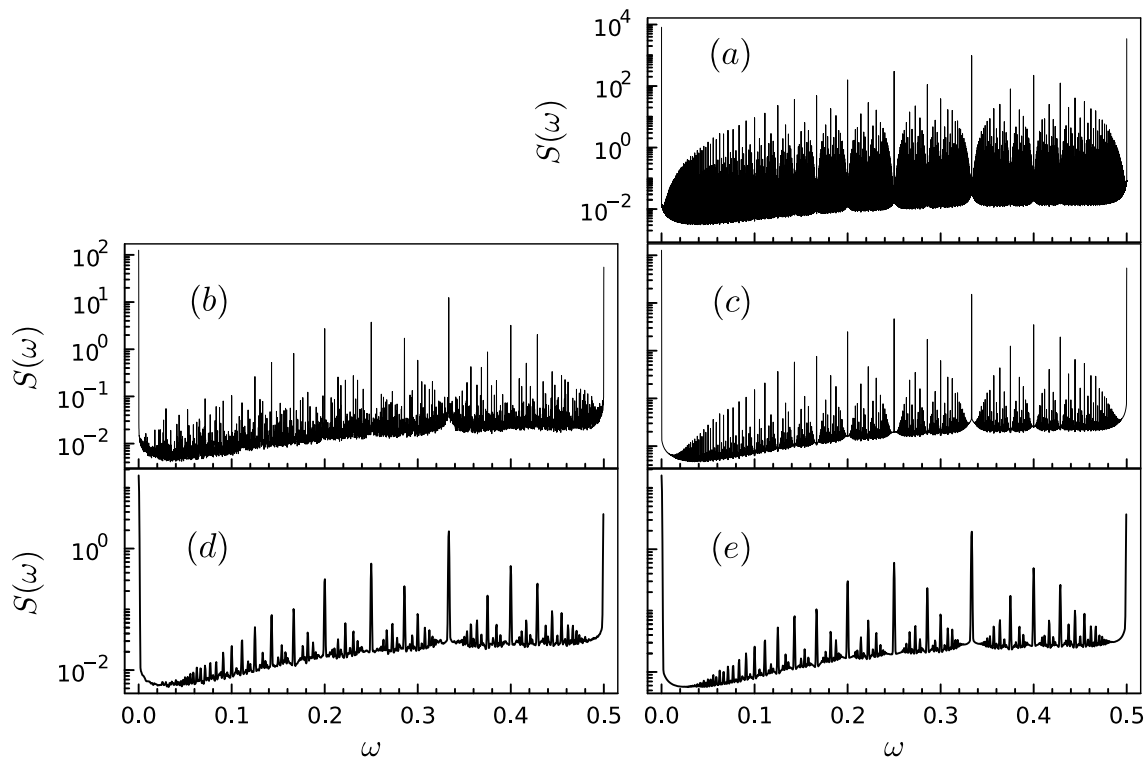
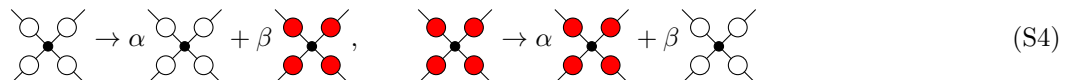


FIG. S5. Power spectra $S(\omega)$ for the $L \times L$ periodic square lattice MCPCA, computed either as time averages (left panels, b,d) over a fixed trajectory (averaged over T_1 sections, each of length T_2 , so that the total duration $T = T_1 T_2$) with a random initial condition, or as a phase space average over many (\mathcal{N}) trajectories with independent random initial conditions (right panels, a,c,e). Panel (a) gives the case $L = 16$, $T = 2^{20}$, $\mathcal{N} = 0.68 \cdot 10^6$ as also shown in the main text, for comparison. Panels (b) and (c) are for lattice size $L = 128$: (b) is for single-trajectory time average with $T_1 = 2^{12}$, $T_2 = 2^{14}$, while (c) is for the phase space average of $\mathcal{N} = 2^{12}$ initial conditions and with trajectory duration $T = 2^{14}$. Panels (d) and (e) are for lattices of size $L = 512$: (d) is for single-trajectory time average with $T_1 = 2^{10}$, $T_2 = 2^{11}$, while (e) is the phase space average of $\mathcal{N} = 2^{10}$ initial conditions and with trajectory duration $T = 2^{11}$.

lattice version of the PCA, and stochastically deform two following two rules:



where $\beta = 1 - \alpha \in (0, 1)$ is the probability that all empty configuration (0000) around the vertex flips to all full (1111), or vice versa. Note that $\beta = 0$ corresponds to a deterministic MCPCA investigated previously, while $\beta = 1$ corresponds to trivial dynamics (flipping all cells at each half-time-step). Such stochastically deformed MCPCA becomes now a bistochastic Markov chain with the same local constants of motion (loop-parities, and Neel loops). Nevertheless, as we demonstrate in Fig S6 the δ -singularities (AC Drude peaks) in $S(\omega)$ are broadened proportionally to β so the power spectrum becomes smooth for any finite value of $\beta \in (0, 1)$.

PCA WITH BROKEN MOMENTUM CONSERVATION

Following up on the question of robustness from the last section, we will now investigate the effect of the breaking of momenta conservation while keeping the parity check and the reversibility intact. In fact, we consider discrete deformations of our PCA update rule Φ_v which map $(s_1, s_2 \dots s_n) \rightarrow (\bar{s}_1, \bar{s}_2 \dots \bar{s}_n)$ for all but one pair of mutually negated configurations which both get mapped to itself $(s'_1, s'_2 \dots s'_n) \rightarrow (s'_1, s'_2 \dots s'_n)$, $(\bar{s}'_1, \bar{s}'_2 \dots \bar{s}'_n) \rightarrow (\bar{s}'_1, \bar{s}'_2 \dots \bar{s}'_n)$. We break momentum conservation if we choose $(s'_1, s'_2 \dots s'_n)$ different from (00...0) or (11...1).

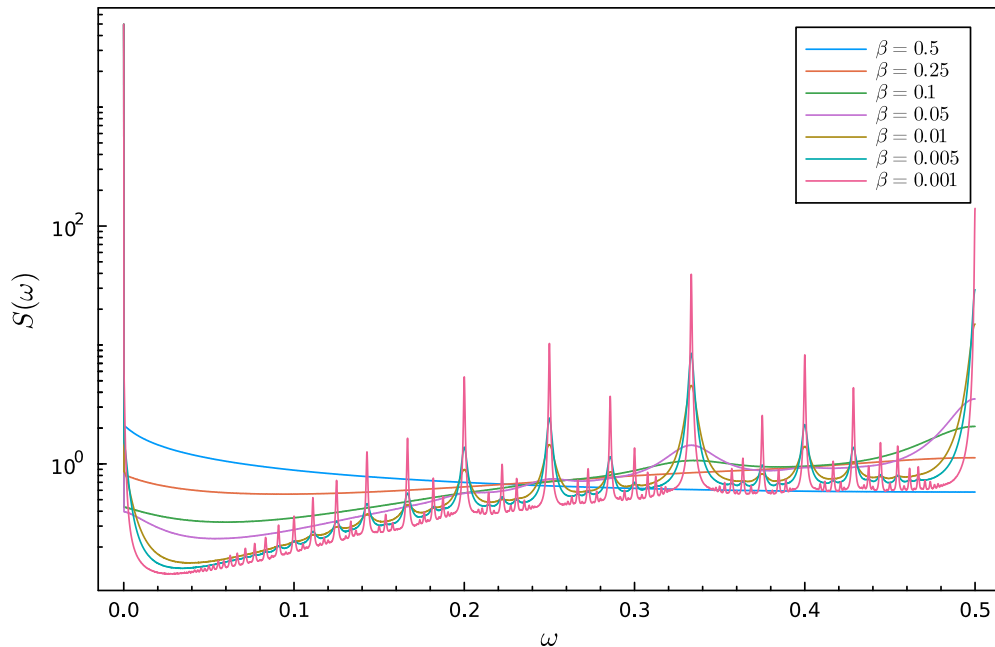
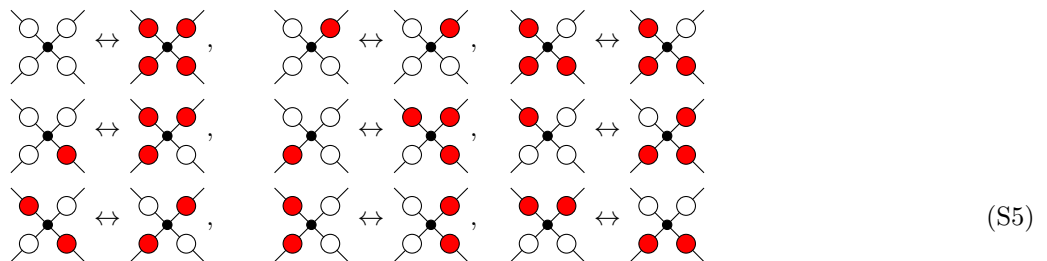


FIG. S6. Power spectra $S(\omega)$ of the density-density autocorrelation function $S(\omega)$ for the stochastically deformed PCA on the square lattice of $N = 2 \times 16^2$ links. β is the probability of stochastically flipping a quadruple of empty/full links (S4). All the plots are calculated for $T = 2^{15}$ with $\mathcal{N} = 2 \cdot 10^5$ initial conditions in the random parity sector $\pi = \pm$.

We consider the following explicit deformation with a complete set of rules:



In fig S7 we show the corresponding power spectra, and demonstrating that it exhibits very similar (if not identical) multifractal spectrum as the MCPCA considered in the main text. Further investigation of the data in figure S8 shows that periodic weights B_p exhibits a power law decay with a similar, if not identical exponent $\mu \approx 1.25$ as that of the original MCPCA on the square lattice in the random parity sector. We also verified that other momentum conservation breaking deformations described above yield essentially identical power spectrum.

Note however that we can also build more complex deformations of MCPCA but still satisfying the parity-check constraint, say such that two (or more) distinct pairs of configurations, $(s_1^{(p)}, s_2^{(p)} \dots s_n^{(p)})$ (and the corresponding negation) map back to themselves, for $p = 1, 2 \dots P$, $P \geq 2$. Quick inspection of power spectra for such PCA models show even distinctly richer structures, depending also on the geometry and dimensionality of the lattice (not shown here). Say for the square lattice and $P = 2$, $S(\omega)$ seem to converge to a continuous but non-smooth function with derivatives experiencing finite jumps at rational frequencies which get smaller with increasing denominators, so a graph of the derivative $S'(\omega)$ may become multifractal.

Finally, what are the effects of deforming the parity-check constraint, i.e. breaking the loop-parity conservation? An old example of a similar cellular automaton with momenta conservation and reversible dynamics is the HPP model [39, 40], which is defined on the square lattice. In addition, this model also conserves the particle number. Clearly, the power spectrum $S(\omega)$ of the HPP model is not multifractal, in fact it has continuous derivatives at all orders (it is a real analytic function). We can then postulate that the all-periodic multifractal response is coming as a result of the interplay between deterministic reversibility and parity check constraint.

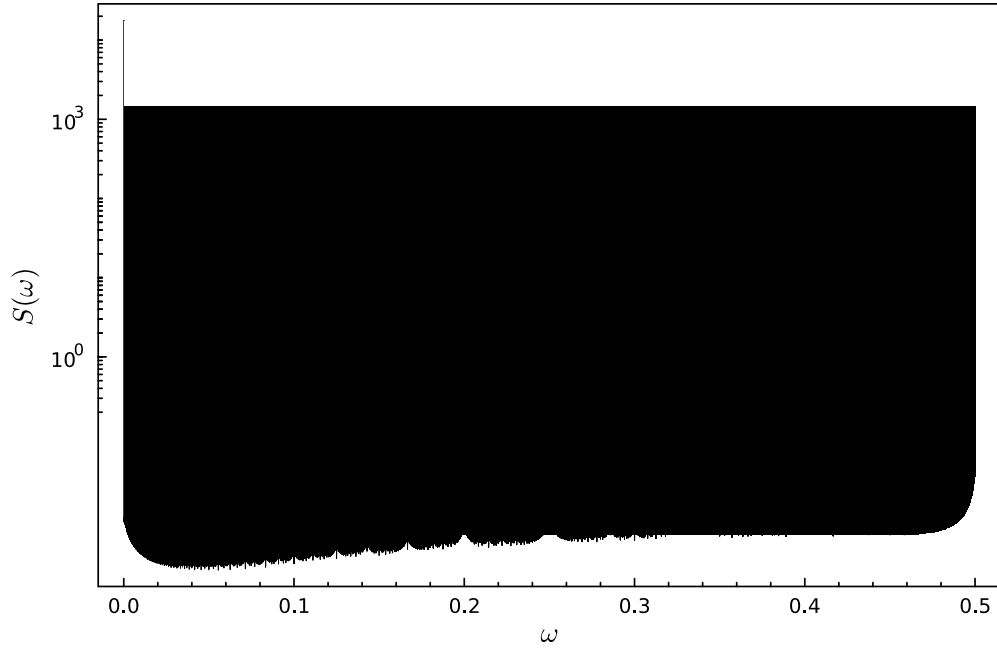


FIG. S7. Power spectrum $S(\omega)$ of the density-density autocorrelation function for the square lattice with size $N = 2 \cdot 16^2$ and for $T = 2^{20}$, for the PCA with broken momentum conservation (S5). The data is averaged over $\mathcal{N} = 4.7 \cdot 10^5$ random initial conditions in the random loop-parity sector $\pi = \pm$.

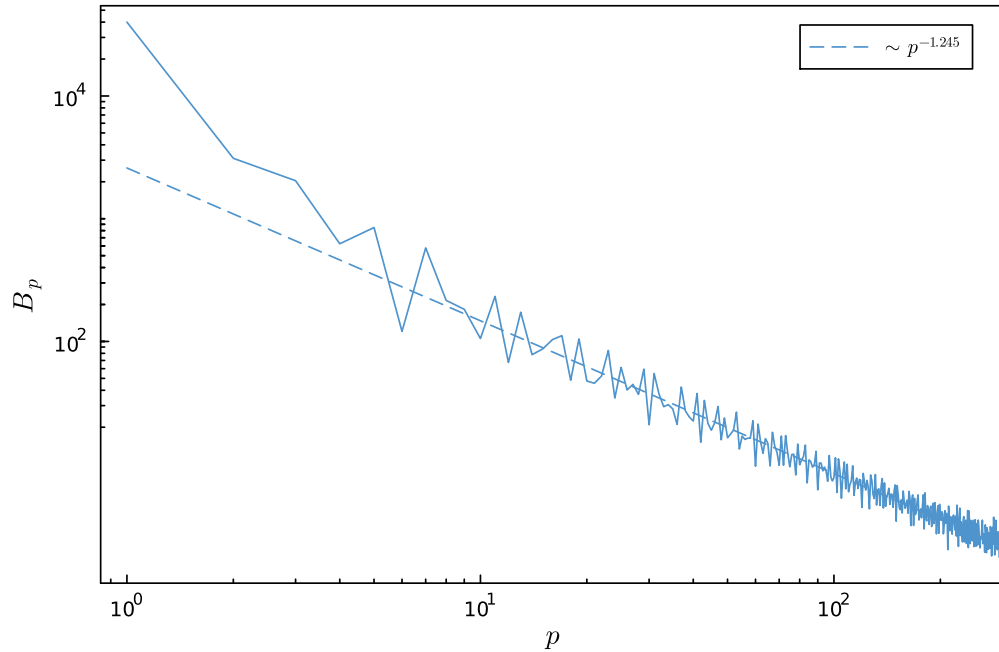


FIG. S8. Spectral weight B_p as a function of the period p in log scale for the square lattice with broken momentum conservation.

GENERALIZED DIMENSIONS OF THE MULTIFRACTAL POWER SPECTRUM

We introduced the generalized dimension D_q in the main text. In fig S9 we plot the generalized dimensions as a function of the moment q for all the three cases of lattices geometries and loop-parity phase space sectors. We also report the values of dimensions D_1 in the following table:

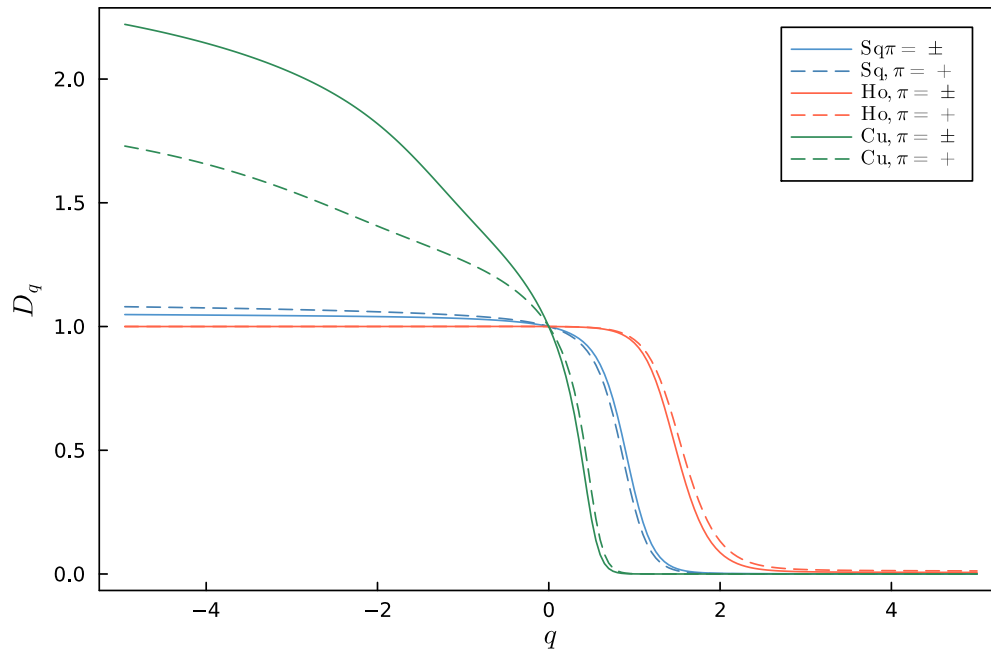
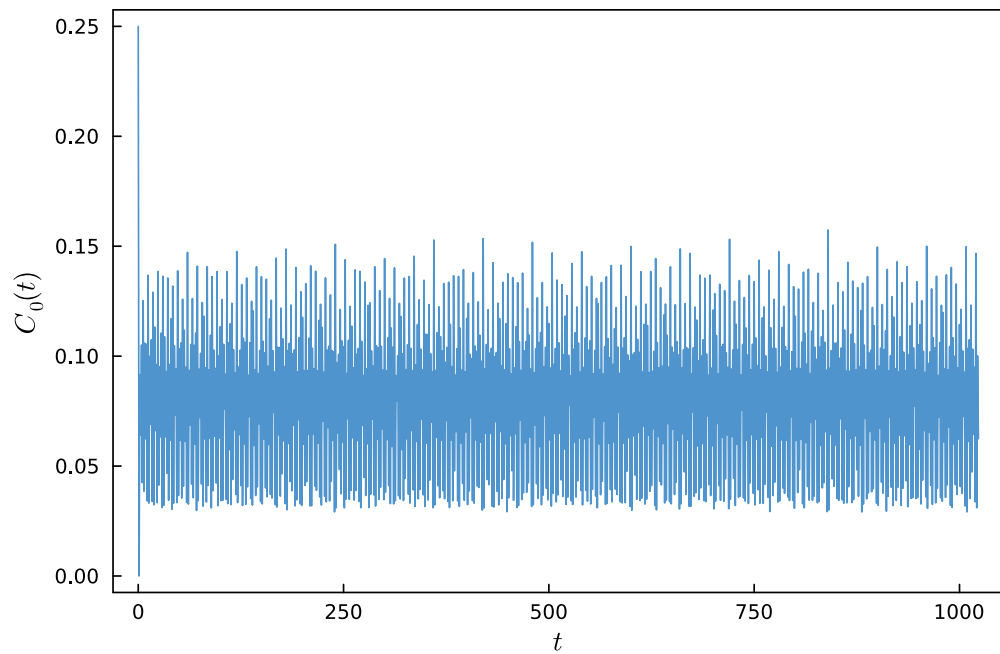


FIG. S9. The generalized dimension D_q as a function of q for different lattices, Sq: square lattice, Ho: honeycomb lattice and Cu: cubic lattice. And for different loop-parity sectors: $\pi = \pm$ random loop-parity sector, and $\pi = +$ positive loop-parity sector.

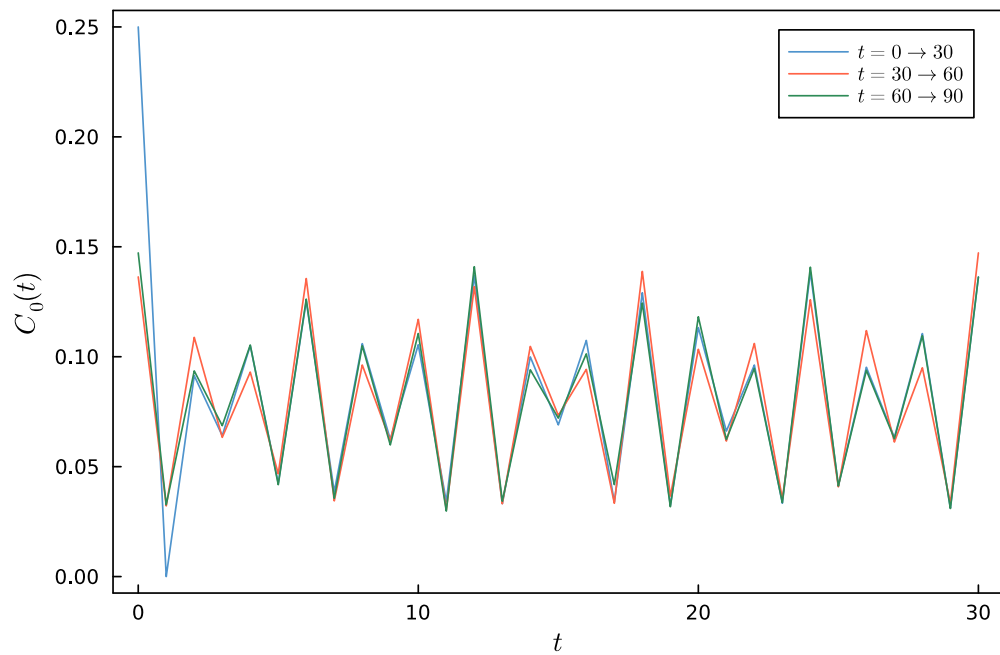
D_1	$\pi = \pm$	$\pi = +$
Sq	0.3965	0.3382
Ho	0.9393	0.9528
Cu	0.0018	0.0028

REAL-TIME AUTOCORRELATION FUNCTIONS

Finally, it may be helpful to illustrate the all-periodic multifractal response by examining the real-time correlation functions. In figure S10(a) we plot the density autocorrelation function at $\vec{r} = 0$ for a 64×64 square lattice up to time $T = 1024$. In figure S10(b) we zoom on the section of $t \in [0, 30]$ we then overlay other time sections of similar length. From the zoomed plot, one can observe the near-but-not-exact-periodicity of each segment. Furthermore, we note an approximate mirror symmetry around time-reflection at the center of time interval.



(a)



(b)

FIG. S10. Density-Density autocorrelation function for the periodic square lattice of size 64×64 , with $N = 2 \times 64^2$ links. Panel (a) shows the autocorrelation up to time $T = 1024$, and panel (b) shows near overlap of the autocorrelation functions for different time windows of fixed length 30: $[0, 30]$, $[30, 60]$, $[60, 90]$.